Thermoelectric transport contribution from topological surface states vs 2D-electron gas in 10 nm Bi₂Se₃ ⊘

Lakshmi Amulya Nimmagadda ⑩ ; Yang Bai; Manjunath C. Rajagopal ⑩ ; Soorya Suresh Babu ⑩ ; James N. Eckstein ⑩ ; Sanjiv Sinha ➡ ⑩



Journal of Applied Physics 132, 164301 (2022) https://doi.org/10.1063/5.0100991





CrossMark





Thermoelectric transport contribution from topological surface states vs 2D-electron gas in 10 nm Bi₂Se₃

Cite as: J. Appl. Phys. 132, 164301 (2022); doi: 10.1063/5.0100991 Submitted: 7 June 2022 · Accepted: 21 September 2022 · Published Online: 24 October 2022







Lakshmi Amulya Nimmagadda, ¹ 📵 Yang Bai, ² Manjunath C. Rajagopal, ¹ 📵 Soorya Suresh Babu, ² 📵 James N. Eckstein,² 匝 and Sanjiv Sinha^{1,3,a)} 匝

AFFILIATIONS

1 Department of Mechanical Science and Engineering, University of Illinois at Urbana-Champaign, Urbana, Illinois 61801, USA
2 Department of Physics, University of Illinois at Urbana-Champaign, Urbana, Illinois 61801, USA
3 Holonyak Micro and Nanotechnology Laboratory, University of Illinois at Urbana-Champaign, Urbana, Illinois 61801, USA
a) Author to whom correspondence should be addressed: sanjiv@illinois.edu

ABSTRACT
Topological surface states (TSSs) coexist with a rapidly formed two-dimensional electron gas (2DEG) at the surface of Bi₂Se₃. While this complex band structure has been widely studied for its interactions between the two states in terms of electrical conductivity and carrier density, the resulting thermopower has not been investigated as thoroughly. Here, we report measurements of the temperature dependent density, the resulting thermopower has not been investigated as thoroughly. Here, we report measurements of the temperature dependent 🛓 Seebeck coefficient (S) and electrical conductivity (σ) on an undoped 10 nm thin Bi₂Se₃ film over the temperature range of 100–300 K to $\frac{5}{2}$ find an overall metal-like behavior. The measured S is consistent with the theory when assuming that both the TSS and the 2DEG contribute to thermoelectric transport. Our analysis further shows that the coefficient corresponds to a Fermi level situated well above the conduction band minima of the 2DEG, resulting in comparable contributions from the TSS and the 2DEG. The thermoelectric power factor ($S^2\sigma$) at 300 K increases by 10%–30% over the bulk. This work provides insights into understanding and enhancing thermoelectric phenomena in topological insulators.

Published under an exclusive license by AIP Publishing. https://doi.org/10.1063/5.0100991

I. INTRODUCTION

Topological insulators are electrical insulators in the bulk that possess highly conducting topological surface states (TSSs) that form under an inverted ordering of the bulk electronic bands due to strong spin-orbit coupling. These surface states exhibit a linear dispersion resulting in massless Dirac fermions, where the electron momentum is locked to its spin, preventing any backscattering due to nonmagnetic impurities. Carrier transport via these states has metal-like conductivities.^{2,3} In Bi₂Se₃, a common thermoelectric material and a topological insulator, these states coexist with a twodimensional electron gas (2DEG) at the surface. Angle-resolved photoemission spectroscopy (ARPES) measurements⁴ have explicitly confirmed this coexistence. The origin of the 2DEG in Bi₂Se₃ is similar to that in other semiconductor surfaces where charge accumulation causes band bending near the surface. While the interactions between TSS and the 2DEG have been extensively studied⁴

for their impact on carrier density, mobility, and conductivity, the thermoelectric properties of the surface arising under this complex band structure are still not well understood.

In experiments on the bulk, it is generally difficult to directly measure the contribution of surface states to thermoelectric transport due to the typically large contributions from the bulk bands⁵ that overwhelm the measurement. In contrast to the bulk, thin films afford a more promising avenue to better understand the thermoelectric properties of TSS in comparison with those of the 2DEG. Magnetoresistance measurements⁶ and terahertz timedomain spectroscopy (THz-TDS) on Bi₂Se₃ films with thicknesses less than 100 nm can distinguish surface charge transport from the bulk but are rare in the literature. Gated measurements of surface thermoelectric transport in thin films of exfoliated Bi₂Se₃ have been reported.⁸⁻¹⁰ In particular, a high $S^2\sigma$ of $3\mu W \text{ cm}^{-1} \text{ K}^{-2}$ was reported at 240 K and a gate voltage of -50 V¹⁰. The value may be attributed to the high Seebeck coefficient resulting from a low

carrier concentration. There was, however, no conclusive evidence in these experiments that the transport was topologically protected. Thus, a physical understanding of the magnitude and temperature dependencies of the thermopower and the thermoelectric power factor when both TSS and 2DEG are present is still lacking.

In extremely thin Bi_2Se_3 films (~ 2 nm), hybridization between the two surfaces is expected to open up a bandgap and also severely reduce the carrier density in the 2DEG. 11,12 This presents an interesting system to explore thermoelectric phenomena. As a step toward this, however, it is also important to understand thermoelectric behavior in slightly thicker films (~10 nm) where both 2DEG and TSS are expected to contribute, effectively forming a two-channel carrier transport.¹³ The spatial extent of surface charge accumulation in the bulk, estimated from the Poisson equation as $\sqrt{\kappa \epsilon_0 \Delta V/en}$ (where κ is the dielectric constant of the bulk, ϵ_0 is the permittivity of vacuum, ΔV is the potential change near the surface, e is the electronic charge, and n is the carrier concentration), yields a figure of ~6 nm at the typically high carrier concentrations $(2.4 \times 10^{19} \text{ cm}^{-3})$ reported in measurements.⁴ More detailed solutions put the decay length to be ~15 nm when the Fermi level is ~160 meV above the conduction band minimum, a typical case.¹⁴ We would thus expect that in films with thicknesses comparable to these figures, surface charge accumulation should create a quantum confined 2DEG across the entire film thickness. The confinement would shift the bottom of the conduction band by $\sim h^2/8m^*t^2$, where h is Planck's constant, m^* is the effective mass, and t is the film thickness. ¹³ At a thickness of 10 nm, the upward shift is ~25 meV. This forms an ideal system to investigate thermoelectric transport where both the 2DEG and the TSS play a role.

Here, we report measurements of S and σ in high-quality Bi₂Se₃ films of 10- and 50-nm thicknesses grown by molecular beam epitaxy (MBE), over the temperature range of 100-300 K to investigate such transport. The 50-nm film serves as a reference with a thermoelectric behavior expected to be essentially identical to that of the bulk. Data from the thicker film also serve to establish the validity of our experimental technique, which is slightly modified from the typical case to improve accuracy. In the thinner film, we expect surface states to be the only channels of transport. Understanding the surface state contribution presents complexities since it includes contributions from both the 2DEG and TSS. As we show below, measurements of the Seebeck coefficient reveal that the Fermi level is well above the conduction band minimum, with the coefficient having contributions from both the 2DEG and the TSS. Analyzing the data, we model transport to enable a relative quantification of the Seebeck coefficient associated with each transport channel. The paper is organized as follows. Section II describes the basic theory of the Seebeck coefficient in the presence of TSS and a 2DEG. Section III outlines the material growth of Bi₂Se₃ films used in our measurements. Section IV describes the measurement platform and the measurement principle used to obtain S and σ . Section V presents the experimental results and discusses the data. Section VI provides conclusions and insights for future work. This work advances the fundamental understanding of thermoelectricity in thin films of topological insulators.

II. DERIVATION OF THE SEEBECK COEFFICIENT

As discussed above, we expect surface band bending in a thin Bi₂Se₃ film with a few-quintuple layers to quantum confine all carriers in the thickness direction, leaving only the 2DEG and the TSS. The Seebeck coefficient for the film is then a weighted sum of the two contributions, $S = (S_{TSS}\sigma_{TSS} + S_{2DEG}\sigma_{2DEG})/$ $(\sigma_{TSS} + \sigma_{2DEG})$. We now derive expressions for the diffusive thermopowers, S_{TSS} and S_{2DEG} , below to help guide the later discussion. We note that we only consider the diffusive part of the thermopower since we do not expect phonon drag to contribute to thermopower. Any momentum transferred from the electrons to phonons is destroyed by boundary scattering in such nanoscale films 1

A. The Seebeck coefficient for TSS

The density of states for TSS is $g(E) = E/2\pi\hbar^2 v_F^2$, where v_F is

$$S_{\text{TSS}} = -\frac{1}{eT} \left(E_F - \int_{0}^{\infty} g(E) \, \tau(E) \, E^2 \, \partial f \, / \partial E \, dE \right), \tag{1}$$

$$S_{\text{TSS}} = -\frac{1}{eT} \left(E_F - \int_{0}^{\infty} \frac{E^{r+3} \partial f / \partial E dE}{\int_{0}^{\infty} E^{r+2} \partial f / \partial E dE} \right). \tag{2}$$

The density of states for TSS is
$$g(E) = E/2\pi\hbar^2 v_F^2$$
, where v_F is the Fermi velocity and \hbar is the reduced Planck constant. The (diffusive) Seebeck coefficient is given by
$$S_{TSS} = -\frac{1}{eT} \left(E_F - \frac{\int_0^\infty g(E) \, \tau(E) \, E^2 \, \partial f \, / \partial E \, dE}{\int_0^\infty g(E) \, \tau(E) \, E \, \partial f \, / \partial E \, dE} \right), \qquad (1)$$
where f is the Fermi function and the relaxation time $\tau(E) \propto E^r$. The above expression simplifies to
$$S_{TSS} = -\frac{1}{eT} \left(E_F - \frac{\int_0^\infty g(E) \, \tau(E) \, E \, \partial f \, / \partial E \, dE}{\int_0^\infty E^{r+3} \, \partial f \, / \partial E \, dE} \right). \qquad (2)$$
The integrals in Eq. (2) can be further simplified using the product rule to yield
$$S_{TSS} = -\frac{1}{eT} \left(E_F - \frac{(r+3) \int_{E=0}^\infty f_0 E^{r+2} \, dE}{(r+2) \int_{E=0}^\infty f_0 E^{r+1} \, dE} \right). \qquad (3)$$
The two integrals in Eq. (3) can be simplified by introducing the reduced energies $\zeta = E/k_B T$, $\eta = E_F/k_B T$, and the Fermi-Dirac by integral defined as $E_F(n) = \int_0^\infty f(E/n) f(E/n) \, dx$. The Seebeck coefficient

the reduced energies $\zeta = E/k_BT$, $\eta = E_F/k_BT$, and the Fermi-Dirac Ξ integral, defined as $F_n(\eta) = \int_0^\infty f_0(\zeta, \eta) \zeta^n d\zeta$. The Seebeck coefficient

$$S_{TSS} = -\frac{1}{eT} \left(E_F - k_B T \frac{(r+3)F_{r+2}(\eta)}{(r+2)F_{r+1}(\eta)} \right)$$
$$= -\frac{k_B}{e} \left(\eta - \frac{(r+3)F_{r+2}(\eta)}{(r+2)F_{r+1}(\eta)} \right). \tag{4}$$

For $\eta \gg 0$, the Fermi-Dirac integral can be expressed in the form of a rapidly converging series where retaining only the first two terms yields

$$S_{TSS} = -\frac{k_B}{e} \left(\eta - \frac{(r+3)F_{r+2}(\eta)}{(r+2)F_{r+1}(\eta)} \right) = -\frac{k_B}{e} \left(\frac{\eta(r+2)F_{r+1}(\eta) - (r+3)F_{r+2}(\eta)}{(r+2)F_{r+1}(\eta)} \right)$$

$$= -\frac{k_B}{e} \left(\frac{\eta(r+2) \left(\frac{\eta^{r+2}}{r+2} + (r+1)\eta^r \frac{\pi^2}{6} \right) - (r+3) \left(\frac{\eta^{r+3}}{r+3} + (r+2)\eta^{r+1} \frac{\pi^2}{6} \right)}{(r+2)\frac{\eta^{r+2}}{r+2}} \right) = -\frac{\pi^2 k_B}{3e} \frac{1}{\eta} (r+2).$$
 (5)

The above expression is linear in temperature, as expected for metals.

The scattering parameter r can be obtained from the relaxation time $\tau(E)$ as follows:

$$\frac{1}{\tau(E_k)} = \sum_{k'} (1 - \cos\theta_{kk'}) W_{kk'} \frac{1 - f(E')}{1 - f(E)},\tag{6}$$

where $\theta_{kk'}$ is the scattering angle between k and k', $E_k = \hbar v_F |k|$, $W_{kk'}$ is the transition probability from the state with momentum kto k' state, and f(E) is the Fermi distribution function. The transition probability is given by $W_{kk'} = 2\pi/\hbar \sum |C(\mathbf{q})|^2 \Delta(E, E')$. C

(q) is the matrix element for scattering by acoustic phonon of wave vector $\mathbf{q} = \mathbf{k} - \mathbf{k}'$ and $\Delta(E, E') = N_q \delta(E - E' + \omega_q) + (N_q + 1)$ $\delta(E - E' - \omega_q)$, where $\omega_q = v_{ph}q$ is the acoustic phonon energy whose velocity is v_{ph} and N_q is the phonon occupation number. The matrix element for the deformation potential is given by

$$|C(\mathbf{q})|^2 = \frac{D^2 \hbar q}{2A\rho_{...} \nu_{ph}} \left[1 - \left(\frac{q}{2k} \right)^2 \right],$$
 (7)

where D is the deformation-potential coupling constant, ρ_m is the mass density, and A is the area of the sample. For temperatures above 100 K, $\hbar\omega_q \ll k_B T$, and consequently, $N_q \approx k_B T/\hbar\omega_q$ and $\Delta(E, E') \approx (2k_BT/\hbar\omega_a)\delta(E-E')$. Using these approximations, the relaxation time is calculated to be

$$\frac{1}{\tau(E_k)} = \frac{1}{\hbar^3} \frac{E_k}{4v_E^2} \frac{D^2}{\rho_w v_{ph}^2} k_B T. \tag{8}$$

From the energy dependence above, the scattering parameter rfor TSS is (-1).

B. The Seebeck coefficient for 2DEG

The Seebeck coefficient of the 2DEG (S_{2D}) is the sum of the Seebeck coefficients of all occupied levels weighted by their individual electrical conductivities. Assuming the mobility to be constant across all levels and independent of carrier concentration, the total Seebeck coefficient can be written as

$$S_{2D} = \frac{\sum_{i} \sigma_{i} S_{2Di}}{\sum_{i} \sigma_{i}} = \frac{\sum_{i} n_{2Di} S_{2Di}}{\sum_{i} n_{2Di}}.$$
 (9)

Here, i is the index of the discrete energy level and n_{2Di} is the occupation of each energy level, given by $n_{2Di} = \int_{1}^{2\pi} \frac{4\pi m^*}{\hbar^2}$ $\times \Phi(E_F - E_i)dE$, where m^* is the effective mass, \hbar is the reduced

Planck constant, E_i is the conduction band edge of the *i*th energy level, and $\Phi(x)$ is the Heaviside step function. The Seebeck coeeficient of each occupied energy level (S_{2Di}) can be derived similarly as above. Using the density of states for a 2DEG as $g(E) = m^*/\pi\hbar^2$ and relaxation time as $\tau(E) \propto E^r$, the diffusive Seebeck coefficient can be written as

$$S_{2Di} = -\frac{1}{eT} \left(E_F - E_i - \int_{E_i}^{\infty} \frac{E^{r+2} \, \partial f / \partial E \, dE}{\int_{E_i}^{\infty} E^{r+1} \partial f / \partial E \, dE} \right)$$

$$= -\frac{1}{eT} \left(E_F - E_i - \int_{0}^{\infty} \frac{E^{r+2} \, \partial f / \partial E' \, dE'}{\int_{0}^{\infty} E'^{r+1} \, \partial f / \partial E' \, dE'} \right). \tag{10}$$

 $E' = E - E_i$. By simplifying the integrals using the product rule and the Fermi-Dirac integral, Eq. (10) can be reduced to

The last part of Eq. (10) arises from the transformation
$$E - E_i$$
. By simplifying the integrals using the product rule and Fermi–Dirac integral, Eq. (10) can be reduced to
$$S_{2\mathrm{D}i} = -\frac{1}{eT} \left(E_F - E_i - \frac{(r+2)\int\limits_0^\infty f_0 E'^{r+1} dE'}{(r+1)\int\limits_0^\infty f_0 E'^r dE'} \right)$$

$$= -\frac{k_B}{e} \left(\eta_i - \frac{(r+2)F_{r+1}(\eta_i)}{(r+1)F_r(\eta_i)} \right). \tag{11}$$

If the Fermi level is high in the conduction bands with $\eta_i \gg 0$, the expression for S_{2Di} reduces similar to Eq. (5) to

$$S_{2Di} = -\frac{\pi^2 k_B}{3e} \frac{1}{\eta_i} (r+1). \tag{12}$$

The relaxation time in the nondegenerate phonon regime for acoustic phonon limited mobility can be written as $\tau(E) \propto 1/g(E)$. Because g(E) is independent of E in a 2DEG, r = 0.17 Consequently, the expression for S is effectively identical for degenerate electrons between the TSS and the 2DEG.

III. MATERIAL GROWTH

We grew the thin-film Bi_2Se_3 on a *c*-plane sapphire (0001) substrate in a UHV chamber ($\leq 10^{-9}$ Torr) using MBE. High-purity Bi (5N) is loaded into an effusion cell and high-purity Se (6N) is loaded into the bulk zone of a valved, cracked selenium source. The fluxes for Bi and Se are set to $1.4-1.5 \times 10^{13}$ and 3.2- 3.7×10^{13} atoms/cm²s, respectively, to achieve super-stoichiometric Se:Bi flux ratios between 4:2 and 5:2. A nucleation layer of six quintuple layers of Bi₂Se₃ is deposited with the substrate temperature set to 80 °C. The substrate temperature is increased to 200 °C to deposit the rest of the film. The substrate temperature is dropped to 100 °C and molecular oxygen is introduced into the chamber at a pressure of 9×10^{-5} Torr. An aluminum beam with a flux of 7×10^{13} atoms/cm² s is used to deposit a 13 Å-thick Al₂O₃ layer on the Bi₂Se₃ surface. This capping protects the film from atmospheric oxidation and helps in reducing selenium vacancies, leading to a lower intrinsic carrier concentration than in an uncapped film. The two nominal film thicknesses chosen in our experiments are 50 and 10 nm. The 50-nm film is expected to exhibit bulklike behavior, whereas the 10-nm film is expected to have transport contributions from different surface states. The sheet carrier density for both films is characterized using Hall bar devices (see Sec. S1 in the supplementary material for sheet carrier density data).

IV. MEASUREMENTS OF S AND σ

To measure S and σ_1 , a Bi₂Se₃ film of lateral dimensions $100 \times 100 \,\mu\text{m}^2$ [Fig. 1(a)] is defined on the substrate by ion milling the sample. The electrodes and heaters are patterned using electron-beam lithography followed by niobium deposition. The contact pads are made of aluminum to ensure good electrical contacts to the sample. The measurement scheme of S is similar to the established methods from the literature¹⁹ but incorporates a few modifications to account for the conductive nature of the films. In the typical measurement scheme, a heater is used to generate a temperature difference (ΔT) across the thin film. ΔT is determined with the help of thin-film resistance temperature detectors (RTDs) (1 and 2) and the corresponding Seebeck voltage (ΔV) is measured as an open circuit voltage across a different set of probes (3 and 4) as shown in Fig. 1(b). Both ΔT and ΔV are measured as a function of the heating voltage applied to the heater (V_H) . Hence, the Seebeck coefficient of the thin film is given by

$$S = -\frac{\Delta V}{\Delta T} = -\frac{d(\Delta V)/d(V_H^2)}{d(\Delta T)/d(V_H^2)}.$$

The spatial difference between the RTDs and the voltage probes in the typical measurement scheme can introduce a significant error in the measurements that is difficult to quantify. To avoid this, we used the same set of probes [1 and 2 in Fig. 1(b)] to measure both $d(\Delta T)/d(V_H^2)$ and $d(\Delta V)/d(V_H^2)$. The RTD probes 1 and 2 are patterned to be in electrical contact with the film since they measure the Seebeck voltage. The RTDs are also used to measure ΔT by measuring the voltages when a sensing current is passed through them and converting them into temperatures using appropriate temperature coefficient of resistance (TCR). However, the electrically conducting nature of the Bi₂Se₃ film leads to leakages in the sensing current, which results in an anomalous behavior of RTDs, such as a negative TCR. To avoid these leakages, the conductive Bi₂Se₃ film was etched away after measuring the Seebeck voltage, as shown in E Fig. 1(c). The details of the calculation of $d(\Delta T)/d(V_H^2)$ can be found in Sec. S2 in the supplementary material.

The electrical conductivity of the 10-nm sample is measured $\frac{8}{8}$ g the standard four-point probe method where current (I) is using the standard four-point probe method where current (I) is passed through the external probes (1 and 2) and voltage (V) is $\frac{\overline{0}}{\overline{0}}$ measured across the internal probes (3 and 4). The probes are equidistant from each other to ensure accurate measurements. The elecdistant from each other to ensure accurate measurements. The elec-

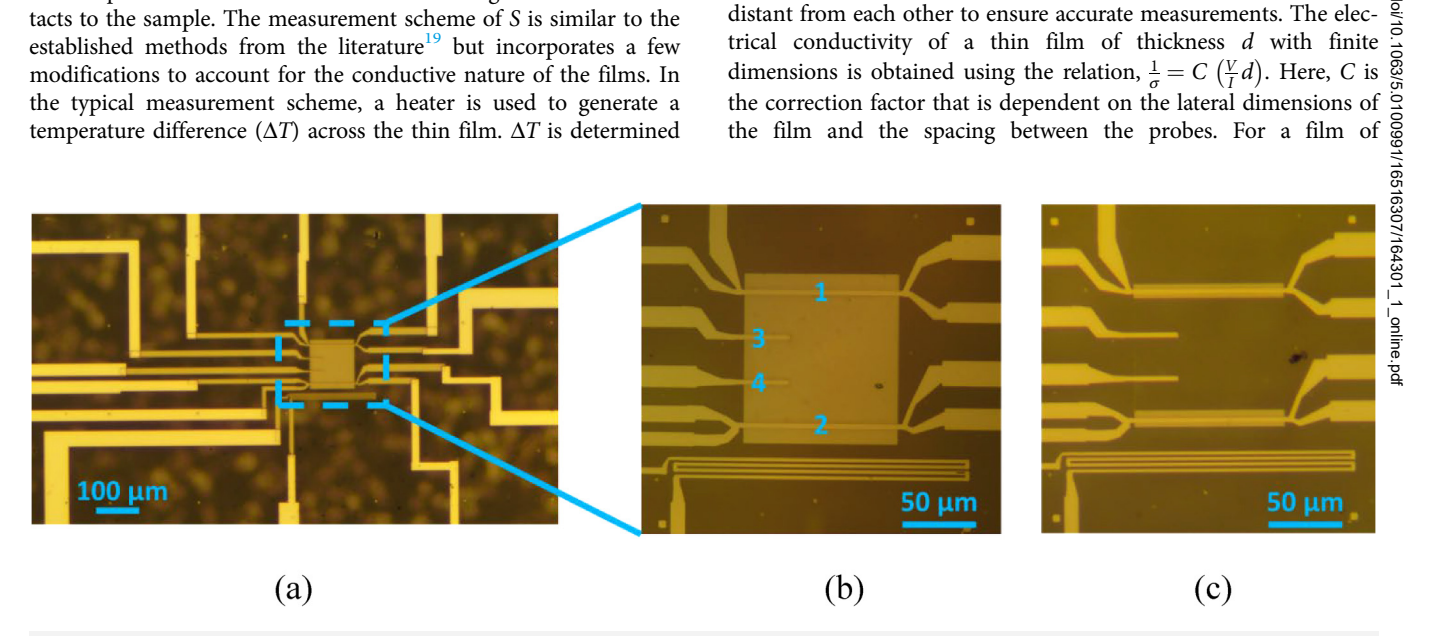


FIG. 1. (a) Optical micrograph of a 10-nm Bi₂Se₃ film with dimensions of 100 × 100 μ m² with electrodes made of niobium and aluminum. (b) Closeup of the thin film sample with Al₂O₃ capping, heater, two RTDs (1 and 2), and two voltage measuring terminals (3 and 4). (c) The thin film sample after selective etching of the Bi₂Se₃ film and the Al₂O₃ capping to enable the measurement of a temperature gradient across the sample.

dimension $100 \times 100 \,\mu\text{m}^2$ and a probe spacing of $\sim 25 \,\mu\text{m}$, $C = 3.1137.^{20}$ (The instrumentation details for the measurement of S and σ are provided in Sec. S3 in the supplementary material.)

V. MEASUREMENT VALIDATION USING 50 nm Bl₂SE₃

Figure 2(a) shows the resistance calibration of the RTDs patterned on the 50 nm Bi₂Se₃ film in the temperature range of 300-350 K. The electrical resistances increase linearly with temperature as expected. Figure 2(b) shows the Seebeck voltage data for the same film at a bath temperature of 330 K, as a function of ΔT across the film. The Seebeck voltage at a given temperature should increase linearly with ΔT , which is indeed observed in the measurements. The slope of the graph provides S of the film at a specific bath temperature. Figure 2(c) shows the measured S as a function of temperature for the 50-nm film. As expected, S is negative, indicating that the material is *n*-type. S increases nonlinearly with temperature in the 50-nm film, indicating semiconducting behavior. The diffusion of charge carriers is the dominant mechanism affecting S. Phonon drag contribution to S is not expected to be significant in this case.^{21,22} At a film thickness of 50 nm, all momentum transferred between electrons and phonons is destroyed by boundary scattering.¹⁵ Then, S due to carrier diffusion can be written as shown in Eq. (1) but with 3D density of states. Because the films are undoped and capped with Al₂O₃ (see Fig. S1 in the supplementary material for carrier density), we may assume negligible impurity scattering. The typical frequencies of optical phonons correspond to temperatures beyond the temperature range of interest (100-350 K), and hence, we can further ignore optical phonon scattering. The dominant scattering is thus from acoustic phonons. With r = -1/2, ²³ S reduces to $S_{3D} = -\frac{1}{e} \left(\eta - 2 \frac{F_1}{F_0} \right)$. Using the carrier concentration data from Fig. S1 in the supplementary

material and $m^* = 0.15 m_e$, 24 E_F is calculated to be ~105 meV $(n = 9.8 \times 10^{18} \text{ cm}^{-3})$ and is almost independent of temperature. S calculated from above is plotted alongside the experimental data for the 50-nm film in Fig. 2(c). The agreement between the data and the established theory for the thick film serves to validate the measurement.

VI. RESULTS AND DISCUSSION

We now discuss the experimental results for the 10-nm film. As pointed out in the Introduction, we expect the band structure to contain only the 2DEG states and the TSS. To explain why, we note that the spatial extent of the quantum well in the 50-nm film at a carrier concentration of $9.8 \times 10^{18} \, \text{cm}^{-3}$ is $\sim \sqrt{\kappa \epsilon_0 \Delta V/en}$ = 8 nm on either surface. This estimate is similar to more detailed, self-consistent calculations of charge accumulation¹⁴ that puts the self-consistent calculations of charge accumulations potential variation near the surface to be ~0.3 eV over ~10 nm. At potential variation near the surface to be ~0.3 eV over ~10 nm. At potential variation near the surface to be ~0.3 eV over ~10 nm. At potential variation near the surface to be ~0.3 eV over ~10 nm. At potential variation near the surface to be ~0.3 eV over ~10 nm. At potential variation near the surface to be ~0.3 eV over ~10 nm. At potential variation near the surface to be ~0.3 eV over ~10 nm. At potential variation near the surface to be ~0.3 eV over ~10 nm. At potential variation near the surface to be ~0.3 eV over ~10 nm. At potential variation near the surface to be ~0.3 eV over ~10 nm. At potential variation near the surface to be ~0.3 eV over ~10 nm. At potential variation near the surface to be ~0.3 eV over ~10 nm. At potential variation near the surface to be ~0.3 eV over ~10 nm. At potential variation near the surface to be ~0.3 eV over ~10 nm. At potential variation near the surface to be ~0.3 eV over ~10 nm. At potential variation near the surface to be ~0.3 eV over ~10 nm. At potential variation near the surface to be ~0.3 eV over ~10 nm. At potential variation near the surface to be ~0.3 eV over ~10 nm. At potential variation near the surface to be ~0.3 eV over ~10 nm. At potential variation near the surface to be ~0.3 eV over ~10 nm. At potential variation near the surface to be ~0.3 eV over ~10 nm. At potential variation near the surface to be ~0.3 eV over ~10 nm. At potential variation near the surface to be ~0.3 eV over ~10 nm. At potential variation near the surface to be ~0.3 eV over ~10 nm. At potential variation near the surface to be ~0.3 eV over ~10 nm. At potential variation near the surface to be ~0.3 eV over ~10 nm. At potential variation near the surface to be ~0.3 eV over ~10 nm. At potential variation near the surface to be ~0.3 eV over ~10 nm. At potential variation near the surface to be ~0.3 eV over ~10 nm. At potential variation near the surface to be ~0.3 e similar doping between the two films, we expect band bending to span the entire thickness of the 10-nm film and the quantum confinement of electrons to create only 2DEG states with TSS in the bandgap. (Hall measurements yielded similar sheet carrier densities in the 10- and 50-nm films, but the equivalent carrier concentration in the 10-nm film would be higher at 3.4×10^{21} cm⁻³.) We thus expect an overall S behavior dictated by S_{TSS} and S_{2D} , weighted by their respective conductivities. Figure 3(a) plots the data for S vs $\frac{w}{2}$ temperature in the 10-nm film. S, while again negative, indicating § transport by electrons, is much lower than that in the 50-nm film. For example, at 300 K, $S = -27.7 \,\mu\text{V/K}$ in the 10-nm film as compared to $-62.4 \,\mu\text{V/K}$ in the 50-nm film. The temperature trend is also different from that in the 50-nm film, with a nearly linear ped dependence suggestive of metallic behavior. As discussed in Sec. II, $\frac{7}{60}$ the linear dependence would arise when S is given by Eqs. (5)

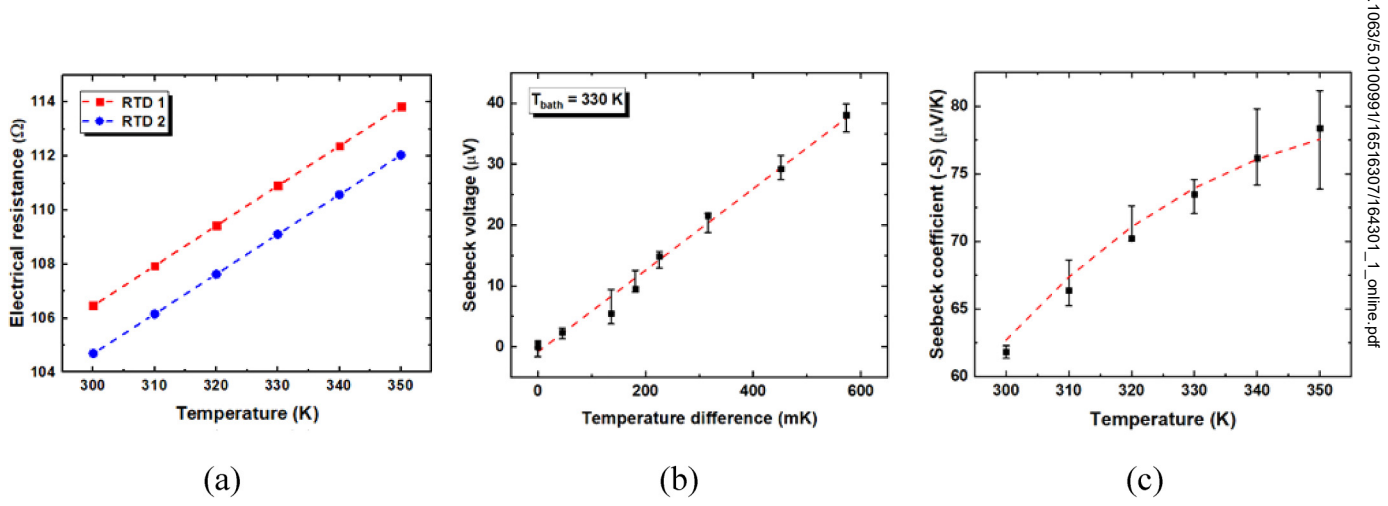


FIG. 2. (a) The measured electrical resistance of the resistance temperature detectors as a function of the environment temperature used in calibration for a 50-nm Bi₂Se₃ film. The error in the resistance is calculated to be between +75 and -8 mΩ and is not included in the graph because of its magnitude when compared with the meaured resistances. (b) Variation of the Seebeck voltage with temperature difference across the sample for the 50-nm-thick Bi₂Se₃ film at a bath temperature of 330 K. The slope of the graph gives the Seebeck coefficient of the sample at 330 K. (c) The experimental Seebeck coefficient of the 50-nm-thick Bi₂Se₃ film as a function of temperature. The red dashed line corresponds to the theoretical Seebeck coefficient calculated for bulk using acoustic phonon scattering as the dominant scattering mechanism.

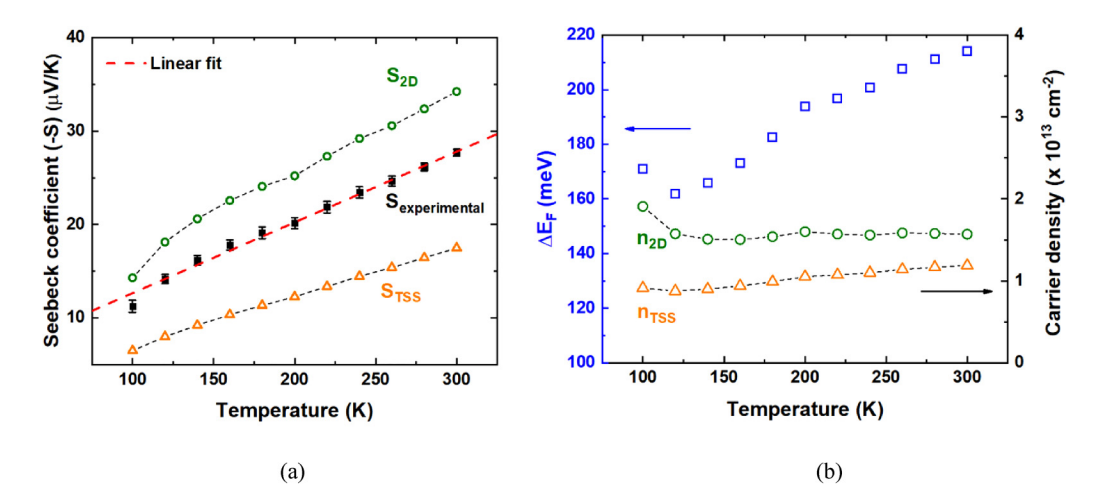


FIG. 3. (a) The Seebeck coefficient of a 10-nm Bi₂Se₃ film measured as a function of temperature. The calculated values of S_{2D} and S_{TSS} are also shown. The measured S is a conductivity weighted average of S2D and STSS. (b) ΔE_F of the 10-nm Bi₂Se₃ film obtained from fitting the measured Seebeck coefficient and the carrier densities of the 2DEG and TSS calculated as a function of temperature.

and (12) for the TSS and the 2DEG, respectively. The situation corresponds to the Fermi level situated high in the 2DEG bands, such that the expression for S_{TSS} and S_{2D} is identical, with each being equal to $-\pi^2 k_B^2 T/3eE_F$. However, the E_F is measured relative to the Dirac Point for the TSS and relative to the conduction band minima for the 2DEG. ARPES data on bulk Bi₂Se₃ shows that the energy gap between the Dirac point of the TSS and the conduction band edge of 2DEG is ~205 meV.4 With quantum confinement in the 10-nm film, we expect the gap to increase slightly. Assuming both surfaces to have similar band bending, a simple estimate of the shift, considering an infinite well, is $\sim h^2/8m^*t^2 = 25$ meV.

Following from the above discussion, we now fit the data using the expression $S = \frac{S_{\text{TSS}} n_{\text{TSS}} \mu_{\text{TSS}} + S_{2D} n_{2D} \mu_{2D}}{(n_{\text{TSS}} \mu_{\text{TSS}} + n_{2D} \mu_{2D})}$, where n is the sheet carrier density and μ is the mobility. The RHS of the expression

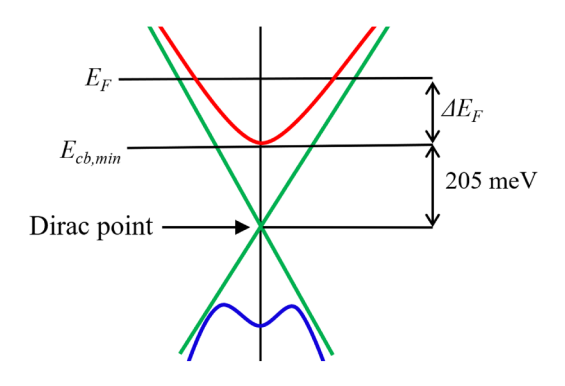


FIG. 4. Schematic representation of the band structure of a 10-nm Bi₂Se₃ film. E_F lies above the conduction band edge of 2DEG, which implies that charge transport takes place through both 2DEG and TSS. The Dirac point is 205 meV below the conduction band edge of 2DEG based on ARPES measurements²

can be rewritten as $(-\pi^2 k_B T/3eE_F) \times \left[\frac{(1/(230+\Delta E_F)+f/\Delta E_F)}{(1+f)}\right]$, where $\Delta E_F = E_F - E_{cb,min}$ and the ratio $f = n_{2D}\mu_{2D}/n_{TSS}\mu_{TSS}$. Our Hall measurements on the 10-nm film show effective carrier density and mobility that are similar to those reported in Ref. 13. In their detailed analysis of the data across multiple samples with varying film thicknesses, the authors reported $\mu_{2D}/\mu_{TSS} \approx 6$ for films of 10-nm thickness. The ratio does not change significantly until a 2-nm thickness. The ratio n_{2D}/n_{TSS} is a function of ΔE_F since each carrier density can be directly calculated by integrating over the states. The carrier density for TSS is given by $n_{TSS} = \frac{(k_B T)^2}{2\pi \hbar^2 v_F^2} F_1(\eta)$. Here, $v_F = 5 \times 10^5$ m/s²⁵ is the Fermi velocity for the topological electronic states in Bi₂Se₃. The 2DEG carrier density is a summation over different quantized states. Employing an empirical effective mass of $0.15 \ m_e^{24}$ over all states, we obtain $n_{2D} = \frac{m^2 k_B T}{\pi \hbar^2} F_0(\eta)$.

Fitting the above expression to the data point by point, we obtain the $\Delta E_F(T)$ plotted in Fig. 3(b). ΔE_F extracted in this manner lies within 170–215 meV. The corresponding location of the Fermi level in the band diagram is shown schematically in $\frac{1}{2}$ and $\frac{1}{2}$ and $\frac{1}{2}$ and $\frac{1}{2}$ and $\frac{1}{2}$ are the location is consistent with degenerate electrons and $\frac{1}{2}$ and $\frac{1}{2}$ and $\frac{1}{2}$ are the location is consistent with degenerate electrons and $\frac{1}{2}$

the Fermi level in the band diagram is shown schematically in Fig. 4. The location is consistent with degenerate electrons and, Fig. 4. The location is consistent with degenerate electrons and, hence, justify the simplifications made in obtaining Eqs. (5) and \(\frac{1}{2} \) (12). This location is also close to but slightly lower than that reported in ARPES^{4,24} measurements of the bulk Bi₂Se₃ surface at carrier concentrations of $\sim 2.4 \times 10^{19} \,\mathrm{cm}^{-3}$. The corresponding carrier densities n_{2D} and n_{TSS} are plotted as a function of temperature in Fig. 3(b), and the corresponding Seebeck coefficients, S_{2D} and S_{TSS} , are plotted in Fig. 3(a). The TSS carrier density is nearly temperature independent, the behavior being consistent with that in prior reports in the literature.¹³ Weighing the two carrier densities by the assumed mobility ratio of $\mu_{2D}/\mu_{TSS} \approx 6$, we obtain a carrier density consistent with those measured in Hall experiments on films (see the supplementary material) prepared under identical conditions to the one for whom S was measured. The carrier

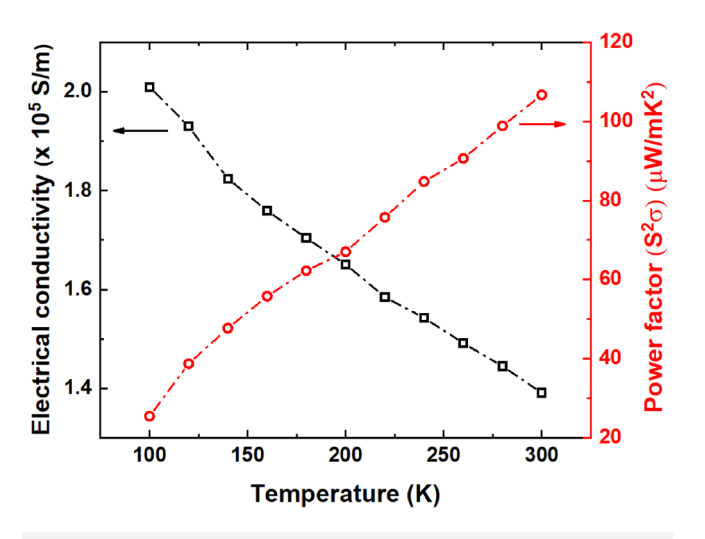


FIG. 5. Electrical conductivity and thermoelectric power factor of a 10-nm Bi₂Se₃ film measured as a function of temperature.

density for the 2DEG has a temperature dependence near the lower temperatures. We are unsure if this is indeed physical or an artifact of the assumptions in our fitting. We note that we have assumed that the mobility ratio remains the same across all temperatures, which is unlikely to be the case at low temperatures where long wavelength phonon scattering can be different between the surface state and the 2DEG.

Figure 5 shows the measured electrical conductivity and the resulting thermoelectric power factor $(S^2\sigma)$ for the 10-nm film. Consistent with a metallic behavior, the overall conductivity decreases as $\sim 1/T$, further confirming the above analysis of a high Fermi level. The power factor at room temperature is modest at $\sim 100 \,\mu\text{W/mK}^2$ and considerably lower than what has been reported earlier in gated measurements. 10 The relatively modest power factor, however, should not be surprising since the carrier density in our sample is quite high. We expect that gated samples are necessary to optimize the power factor. Overall, the power factor is still almost 30% higher than that expected in as-grown bulk Bi₂Se₃.²⁶ The high electrical conductivity is primarily responsible for this enhancement. Even though their S is lower than that found in bulk samples, surface conduction through the 2DEG and the TSS still yields a higher $S^2\sigma$.

VII. CONCLUSIONS

In conclusion, we have experimentally measured the Seebeck coefficient and electrical conductivity of a 10-nm thin Bi₂Se₃ film. Through theoretical analysis, we suggest that the entire film is comprised of surface states in the form of 2DEG and TSS. Comparing with measurements on a thicker 50-nm film, we find that in the thinner film, thermoelectric transport is surface dominated and metal-like, with comparable contributions from the TSS as well as the 2DEG. The overall behavior is metallic and consistent with a Fermi level located high in the 2DEG bands. Overall, surface

conduction leads to an increase in σ and a decrease in S compared with the bulk but with an overall higher $S^2\sigma$. These results present insights into further increasing the $S^2\sigma$ of TSS by controlling the band structure of the TSS at lower film thicknesses. We note that theory¹¹ and experiments¹² show that a bandgap opens in the TSS at thicknesses 2 nm and lower due to hybridization of the two surfaces. This has the potential to provide a simultaneously high power factor and conductivity, which is an important attribute in realizing practical, high-quality thermoelectric-based heat switches.²

SUPPLEMENTARY MATERIAL

See the supplementary material for the experimental details and measured data of carrier concentration, mobility, the Seebeck coefficient, and electrical conductivity and methodology used to determine the Seebeck coefficient.

ACKNOWLEDGMENTS

Quantum Leap Challenge Institute for Hybrid Quantum & Architectures and Networks (NSF Avord NT 2021) M.C.R., and S.S. acknowledge partial funding for this work from

M.C.R., and S.S. acknowledge partial funding for this work from the Intel Corporation.

AUTHOR DECLARATIONS

Conflict of Interest

The authors have no conflicts to disclose.

Author Contributions

Lakshmi Amulya Nimmagadda: Conceptualization (equal); Formal analysis (equal); Investigation (equal); Methodology (equal); Validation (equal); Writing – original draft (equal); Writing – review & editing (equal). Yang Bai: Investigation (equal); Methodology (equal); Methodology (equal). Manjunath C. Rajagopal: Investigation (supporting); Methodology (supporting); Writing – review & editing (supporting). Soorya Suresh Babu: Investigation (supporting); Methodology (supporting); Supervision (supporting). Sanjiv Sinha: Conceptualization (equal); Investigation (equal); Methodology (equal); Supervision (equal); Methodology (equal); Supervision (equal); Investigation (equal); Methodology (equal); Supervision (equal); Methodology (equal); Methodolog Writing – review & editing (equal).

DATA AVAILABILITY

The data that support the findings of this study are available within the article and its supplementary material.

REFERENCES

¹X.-L. Qi and S.-C. Zhang, Rev. Mod. Phys. **83**, 1057 (2011).

²Y. Xia, D. Qian, D. Hsieh, L. Wray, A. Pal, H. Lin, A. Bansil, D. Grauer, Y. S. Hor, R. J. Cava, and M. Z. Hasan, Nat. Phys. 5, 398 (2009).

³Y. L. Chen, J. G. Analytis, J.-H. Chu, Z. K. Liu, S.-K. Mo, X. L. Qi, H. J. Zhang, D. H. Lu, X. Dai, Z. Fang, S. C. Zhang, I. R. Fisher, Z. Hussain, and Z.-X. Shen, Science 325, 178, (2009).

⁴M. Bianchi, D. Guan, S. Bao, J. Mi, B. B. Iversen, P. D. C. King, and P. Hofmann, Nat. Commun. 1, 128 (2010).

⁶J. Chen, X. Y. He, K. H. Wu, Z. Q. Ji, L. Lu, J. R. Shi, J. H. Smet, and Y. Q. Li, Phys. Rev. B **83**, 241304 (2011).

⁷V. S. Kamboj, A. Singh, T. Ferrus, H. E. Beere, L. B. Duffy, T. Hesjedal, C. H. W. Barnes, and D. A. Ritchie, ACS Photonics 4, 2711 (2017).

⁸D. Kim, Q. Li, P. Syers, N. P. Butch, J. Paglione, S. D. Sarma, and M. S. Fuhrer, Phys. Rev. Lett. **109**, 166801 (2012).

⁹D. Kim, S. Cho, N. P. Butch, P. Syers, K. Kirshenbaum, S. Adam, J. Paglione, and M. S. Fuhrer, Nat. Phys. 8, 459 (2012).

¹⁰D. Kim, P. Syers, N. P. Butch, J. Paglione, and M. S. Fuhrer, Nano Lett. 14, 1701 (2014).

¹¹P. Ghaemi, R. S. K. Mong, and J. E. Moore, Phys. Rev. Lett. **105**, 166603 (2010).

12Y. Zhang, K. He, C.-Z. Chang, C.-L. Song, L.-L. Wang, X. Chen, J.-F. Jia, Z. Fang, X. Dai, W.-Y. Shan, S.-Q. Shen, Q. Niu, X.-L. Qi, S.-C. Zhang, X.-C. Ma, and Q.-K. Xue, Nat. Phys. 6, 584 (2010).

¹³N. Bansal, Y. S. Kim, M. Brahlek, E. Edrey, and S. Oh, Phys. Rev. Lett. **109**, 116804 (2012).

¹⁴M. S. Bahramy, P. D. C. King, A. de la Torre, J. Chang, M. Shi, L. Patthey, G. Balakrishnan, P. Hofmann, R. Arita, N. Nagaosa, and F. Baumberger, Nat. Commun. 3, 1159 (2012).

¹⁵J. Sadhu, H. Tian, J. Ma, B. Azeredo, J. Kim, K. Balasundaram, C. Zhang, X. Li, P. M. Ferreira, and S. Sinha, Nano Lett. 15, 3159 (2015).

¹⁶E. H. Hwang and S. Das Sarma, Phys. Rev. B 77, 115449 (2008).

¹⁷B. K. Ridley, B. E. Foutz, and L. F. Eastman, Phys. Rev. B **61**, 16862 (2000).

¹⁸B. T. Mulcahy, *The Superconducting Proximity Effect in Bi₂Se₃ Thin-Films* (Ph.D., University of Illinois at Urbana-Champaign, 2015).

¹⁹J. P. Small, K. M. Perez, and P. Kim, Phys. Rev. Lett. **91**, 256801 (2003).

²⁰F. M. Smits, Bell Syst. Tech. J. **37**, 711 (1958).

²¹C. Herring, Phys. Rev. **96**, 1163 (1954).

²²L. Weber and E. Gmelin, Appl. Phys. A **53**, 136 (1991).

²³M. Lundstrom, in *Fundamentals of Carrier Transport*, 2nd ed. (Cambridge University Press, Cambridge, 2000).

²⁴J. G. Analytis, J.-H. Chu, Y. Chen, F. Corredor, R. D. McDonald, Z. X. Shen, and I. R. Fisher, Phys. Rev. B 81, 205407 (2010).

²⁵Z.-H. Zhu, G. Levy, B. Ludbrook, C. N. Veenstra, J. A. Rosen, R. Comin, D. Wong, P. Dosanjh, A. Ubaldini, P. Syers, N. P. Butch, J. Paglione, I. S. Elfimov, and A. Damascelli, Phys. Rev. Lett. 107, 186405 (2011).

²⁶Y. Sun, H. Cheng, S. Gao, Q. Liu, Z. Sun, C. Xiao, C. Wu, S. Wei, and Y. Xie, J. Am. Chem. Soc. 134, 20294 (2012).

²⁷M. J. Adams, M. Verosky, M. Zebarjadi, and J. P. Heremans, Int. J. Heat Mass Transfer 134, 114 (2019).